PAPER

Check for updates

Electrochemical trends of a hybrid platinum and metal–nitrogen–carbon catalyst library for the oxygen reduction reaction†

Alvin Ly,‡[a] Eamonn Murphy, ‡[b] Hanson Wang,‡[b] Ying Huang, [a] Giovanni Ferro,[b] Shengyuan Guo, [b] Tristan Asset,[c] Yuanchao Liu,[b] Iryna V. Zenyuk [ab] and Plamen Atanassov*[ab]

Enhancing the activity and durability of Pt nanoparticles for the oxygen reduction reaction (ORR) is of critical importance in achieving an optimal, cost-efficient proton exchange membrane fuel cell (PEMFC) catalyst. Aimed at improving the intrinsic catalytic activity and durability of the Pt nanoparticles, this work utilizes a library of fourteen 3d, 4d, 5d, and *f* metal atomically dispersed metal–nitrogen–carbon (M–N–C) catalysts as active supports, synthesizing a corresponding library of Pt/M–N–C catalysts. XPS and XANES measurements indicate a reduced oxidation state of the Pt nanoparticles due to interactions with the M–N–C support. Further alteration of the electronic structure of the Pt nanoparticles arising from interactions with the M–N$_x$ sites is evidenced through the CO oxidation peak, which experiences broadening, shoulder formation and peak shifting over varying M–N–C supports. ORR performance reveals the significantly enhanced intrinsic catalytic activity of the Pt nanoparticles on M–N–Cs over a Pt/C standard, through specific activity calculations. This work demonstrates the application of highly active hybrid Pt/M–N–C catalysts, showcasing the variation in activity as one traverses the periodic table, while highlighting important design criteria to achieve highly active and durable ORR catalysts.

Broader context

Proton exchange membrane fuel cells (PEMFC) are a promising renewable alternative to fossil fuel-based transportation, particularly with respect to long haul trucking. The high cost of platinum (Pt), combined with the high loadings required for sustained performance and inadequate durability limits the widespread deployment of PEMFCs. Atomically dispersed metal–nitrogen–carbon (M–N–C) catalysts have shown strong oxygen reduction reaction (ORR) performance, while significantly reducing metallic content, due to a maximized atom utilization. However, M–N–C catalysts often suffer from reduced durability. In this work, we synthesize a library of hybrid Pt/M–N–C catalysts, exploring 3d, 4d, 5d and f metals, highlighting the unique interactions between the M–N$_x$ site and Pt nanoparticles. The Pt/M–N–C ORR performance demonstrates a significantly enhanced intrinsic specific activity of the Pt nanoparticles interacting with the supporting M–N$_x$ sites, however, durability studies highlight the importance of the carbon structure in the underlying M–N–C support. This work provides a platform for creating highly tailorable Pt/M–N–C systems, in which the metal center can be tuned to alter the electronic structure of the Pt nanoparticles, increasing catalytic activity. While also demonstrating the importance of a more graphitic carbon structure of the M–N–C for enhanced durability.

a Department of Materials Science and Engineering, National Fuel Cell Research Center (NFCRC), University of California-Irvine, Irvine, California 92697, USA. E-mail: plamen.atanassov@uci.edu

b Department of Chemical and Biomolecular Engineering, National Fuel Cell Research Center (NFCRC), University of California-Irvine, Irvine, California 92697, USA

c Institute of Chemistry and Processes for Energy, Environment and Health (ICPEES), UMR 7515 CNRS-Université de Strasbourg, 25 rue Becquerel, Strasbourg Cedex 02 67087, France

† Electronic supplementary information (ESI) available. See DOI: https://doi.org/10.1039/d3ey00235g

‡ Authors contributed equally to this work.

Introduction

Significant global research efforts have been aimed at the decarbonization of the transportation and energy sector, with proton exchange membrane fuel cells (PEMFC), presenting an alternative to traditional fossil fuel-based technologies. Although PEMFCs are becoming increasingly viable alternatives, a major drawback remains the use of expensive catalysts to drive the sluggish cathodic oxygen reduction reaction (ORR) at sufficiently high rates.[1–3] While platinum (Pt) based catalysts remain the best performing materials for the ORR, numerous efforts have been made to reduce the amount of Pt used or

improve the intrinsic activity of the Pt. Although these efforts have made significant advancements in the field, the high price and scarcity of Pt remains a major roadblock for the deployment and wide-spread commercial use of PEMFCs.[4,5]

As a more sustainable alternative to Pt based materials, extensive efforts have been aimed at the development of highly active and stable platinum-group-metal (PGM) free catalysts.[4,6–9] The most reported of this class are atomically dispersed metal–nitrogen–carbon (M–N–C) catalysts, which have made commendable progress. However, despite the rapid improvements of M–N–C catalysts, a major drawback remains the activity and durability issues, which must be improved prior to its commercial deployment.[10,11]

Recently, aimed at increasing the intrinsic activity and durability of the Pt nanoparticles, it has been hypothesized that by utilizing M–N–C materials as an active support for the Pt nanoparticles, electron donation from the $M–N_x$ sites to the more electrophilic Pt nanoparticles could yield increased activity and durability of the hybrid Pt/M–N–C catalysts over traditional Pt/C or M–N–C catalysts.[12–14] Experimental reports of Pt/M–N–C catalyst have only recently been reported in the literature, and are generally divided into two approaches to achieve synergistic effects: the use of Pt nanoparticles at an ultra-low loading as an additive for M–N–C catalysts or the substitution of the carbon support with an M–N–C material for typical higher loading Pt-based catalysts. The first approach utilizes Pt as an additive to leverage the nature of Pt as a strong peroxide scavenger, which prevents the rapid degradation of the M–N–C catalyst due to the production of caustic hydrogen peroxide through the parasitic $2e^- + 2e^-$ transfer pathway (compared with the ideal $4e^-$ transfer pathway leading only to the formation of water).[15–20] In the second approach, the substitution of the carbon support, with an M–N–C material replaces an ORR inactive carbonaceous support material with a material that has an intrinsic activity for the ORR to improve the catalyst layer performance or alter the electronic structure of the Pt nanoparticles through Pt nanoparticle-$M–N_x$ interactions, enhancing the ORR activity.[12,14,21–23] Recently, work from Qiao *et al.* and Liang *et al.*, demonstrated that the strong interactions occurred between the $M–N_x$ sites of the M–N–C support material and the Pt nanoparticles, which were attributed to the observed activity and durability improvements.[14,15] The strength and nature of the Pt nanoparticle–$M–N_x$ interactions could be tuned for enhanced ORR performance (*i.e.*, optimizing reactant or intermediate adsorption energies) by tailoring the $M–N_x$ center, either through ligand field effects or by changing the metal center(s) in the $M–N_x$ site.

Here, we employ a library of 14 atomically dispersed M–N–C catalysts, with 3d, 4d, 5d, and f metal centers to synthesize a corresponding library of 14 Pt-decorated M–N–C catalysts, Pt/M–N–C. Electron microscopy confirms the simultaneous presence of atomically dispersed Pt nanoparticles (2–5 nm) on top of atomically dispersed $M–N_x$ sites. Chemical analysis reveals an electron donating behavior of the M–N–C support to the Pt nanoparticles, reducing the Pt oxidation state. The ORR behavior of the M–N–C supports is first analyzed, highlighting

the superior behavior of the Fe–N–C and Rh–N–C materials. The ORR performance of the Pt/M–N–C catalysts is then examined, resulting in half wave potentials ($E_{1/2}$) up to 0.91 V *vs.* RHE. CO stripping measurements again highlight the unique interactions of the $M–N_x$ sites on the electronic structure of the Pt nanoparticles, leading to peak shifts and shoulder formations in the CO oxidation peaks, with the creation of sites that either promote or inhibit CO oxidation, based on the $M–N_x$ site. The Pt/M–N–C catalysts showed competitive mass activities (M_A) over 230 A g_{Pt}^{-1} as compared to standard Pt/C catalysts. The intrinsic catalytic activity, represented by the specific activity (S_A) of the Pt/M–N–C, Pt nanoparticles, was significantly enhanced up to 670 μA cm^{-2} as compared to 400 μA cm^{-2} for standard Pt/C. Durability measurements following both a more mild drive cycle protocol (0.6–1.0 V *vs.* RHE) and harsher start-up shut-down protocol (1.0–1.5 V *vs.* RHE) highlighted a critical design consideration when synthesizing Pt/M–N–C catalysts. The Pt/M–N–C catalysts demonstrated a high durability in the lower potential regime, while suffering from significant carbon corrosion and loss of ECSA in the higher potential regime. Despite the degradation, the S_A of the Pt/M–N–C catalyst remains extremely high, 6× higher than Pt/C. The issue of durability is linked to the stability of the carbon matrix in which the $M–N_x$ sites are anchored, with the lower graphic content of the M–N–Cs leading to increased carbon corrosion as compared to the graphitic carbon support of the standard Pt/C. This presents a clear target to not only maintain the increased intrinsic ORR activity of the Pt/M–N–C catalysts, but also improve the durability by synthesizing M–N–C based supports with a larger graphic content. This work demonstrates the unique range of Pt/M–N–C catalysts that can be synthesized, while highlighting the unique interaction of the $M–N_x$ sites on the Pt nanoparticles, and elucidating important design criteria, presenting a viable strategy for synthesizing highly active and durable hybrid Pt/M–N–C ORR catalysts.

Results and discussion

Synthesis and characterization of materials

Atomically dispersed M–N–C materials were synthesized *via* the robust sacrificial support method (SSM), originally developed by our group.[24–26] The SSM has been regularly practiced for first row transition metals and utilized for the ORR, carbon dioxide reduction, and reduction of nitrogen species.[27,28] Recently, we extended the SSM to include 4d, 5d and f-metals and synthesized a set of 13 M–N–C catalysts (M = Cr, Mn, Fe, Co, Ni, Cu, Mo, Ru, Rh, Pd, La, Ce and W) for the reduction of nitrogen oxides.[29] Here, we have utilized this set of M–N–C's, and introduced a Pt–N–C sample, comprising a library of 14 M–N–C materials and a metal free N–C catalyst.

The SSM is described in detail in the methods section and shown schematically in the top section of Fig. 1. Briefly, a mixture of nicarbazin, nanoporous silica, and a metal salt precursor are pyrolyzed in a reductive atmosphere, impregnating the pores of the nanoporous silica prior to complete
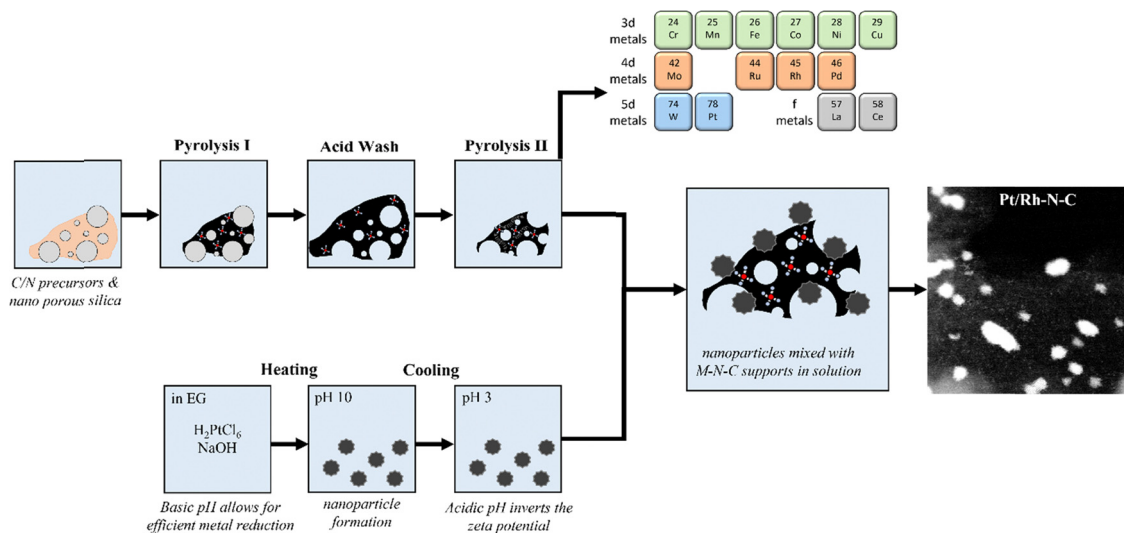
Fig. 1 Synthesis of the Pt/M−N−C samples. The sacrificial support method (top) is used to synthesize atomically dispersed M−N−C supports. The selection of M−N−C catalysts used in this work is shown in the top right. A microwave-assisted polyol method with chloroplatinic acid is used for the synthesis of the Pt nanoparticles.

carbonization. An acid wash in HF is used to remove the sacrificial silica template and any metallic nanoparticles. A second pyrolysis in an ammonia atmosphere removes any fluorinated species, increases defects, etches micropores, and disperses possible nanoclusters, increasing catalyst activity. The Pt nanoparticles are synthesized in a large-scale batch (to avoid issues of batch-to-batch variation) based on a previously reported, adapted version of the classical polyol method. These nanoparticles have an average size of *ca.* 2–5 nm in diameter with a uniform size distribution and active surfaces that are easily cleaned *via* electrochemical potential cycling as large surfactants are not used in this synthesis approach. The microwave assisted polyol method is shown in the bottom section of Fig. 1. The Pt precursor is dispersed in ethylene glycol and transitioned to alkaline pH for efficient reduction of the Pt ions, through the addition of 1 M NaOH. The solution was heated to 180 °C and held for 20 min. Finally, the solution was adjusted to an acidic pH (adding 1 M H_2SO_4), pH 3, to prevent further reduction. The Pt particles are then supported on either XC72R or an M−N−C (or metal free N−C) by mixing the nanoparticles and support material in a 50/50 mixture of water/ethylene glycol and stirred for 24 hours, followed by vacuum filtration, and dried at 60 °C. The targeted Pt loading is *ca.* 20 wt%.

The synthesis parameters were optimized to maintain an atomic dispersion for each metal element of the M−N−C materials (see Methods section). Aberration corrected AC high angle annular dark field scanning transmission electron microscopy (AC-HAADF-STEM) images are shown in Fig. 2a–e. Fig. 2a and b show the Pt/Rh−N−C catalyst, where Pt nanoparticles and Rh single atoms are simultaneously observed, confirming the Rh remains as single atoms after the Pt deposition. Additional TEM images showing the Pt particle size on XC72R *vs.* an M−N−C are provided in Fig. S1 (ESI†). While additional low and high mag STEM images of the Pt/Rh−N−C are provided in Fig. S2

(ESI†). Energy dispersive X-ray spectroscopy (EDS) elemental mapping is also presented in Fig. S3 (ESI†), confirming the presence of Pt nanoparticles and a homogenous dispersion of Rh, N and C, from the Rh−N−C support. Fig. 2c–e shows representative M−N−C catalysts, for a 3d metal (Mn−N−C), 4d metal (Rh−N−C), and f metal (Ce−N−C), where in each image the atomically dispersed metal sites are observed, confirming an atomic dispersion of the metal.

X-ray diffraction (XRD) was used as one approach to confirm the absence of metal nanoparticles in the Pt−N−C support (as confirmed for the other M−N−Cs in a recent work[29]) and to investigate the crystalline phases of the Pt nanoparticles and carbon structure of the catalysts. Fig. 3a shows show only the (002) and (100) carbon peaks for the Pt−N−C, N−C and XC72R samples, demonstrating the absence of crystalline metallic nanoparticles. The XRD pattern for the Pt nanoparticle containing catalysts show the presence of the (111), (200), (220) and (311) facets. The carbon structure of the support materials (XC72R, N−C and Pt−N−C) were further investigated through Raman spectroscopy. The deconvoluted spectra are shown in Fig. 3b, where the D/G ratio of each support is given. By comparing the D/G intensity ratios, the XC72R support (D/G = 0.94) is shown to be more graphitic over the metal free N−C (1.16) and atomically dispersed Pt−N−C (1.17) supports, synthesized using the SSM. N_2-physisorption was used to evaluate the pore size distribution and surface area of the M−N−C supports, where a dominating mesoporosity with 2 peaks (*ca.* 20 nm and *ca.* 65 nm) are observed, characteristic of the sacrificial nanoporous silica template. A surface area of *ca.* 600 m² g⁻¹ is observed for both the metal free N−C and Pt−N−C sample, consistent with the other M−N−C's reported in our previous work.[29]

X-ray photoelectron spectroscopy (XPS) was used to probe the N-moieties in the M−N−C supports. Fig. 3d shows a breakdown of the different nitrogen species present in the library of
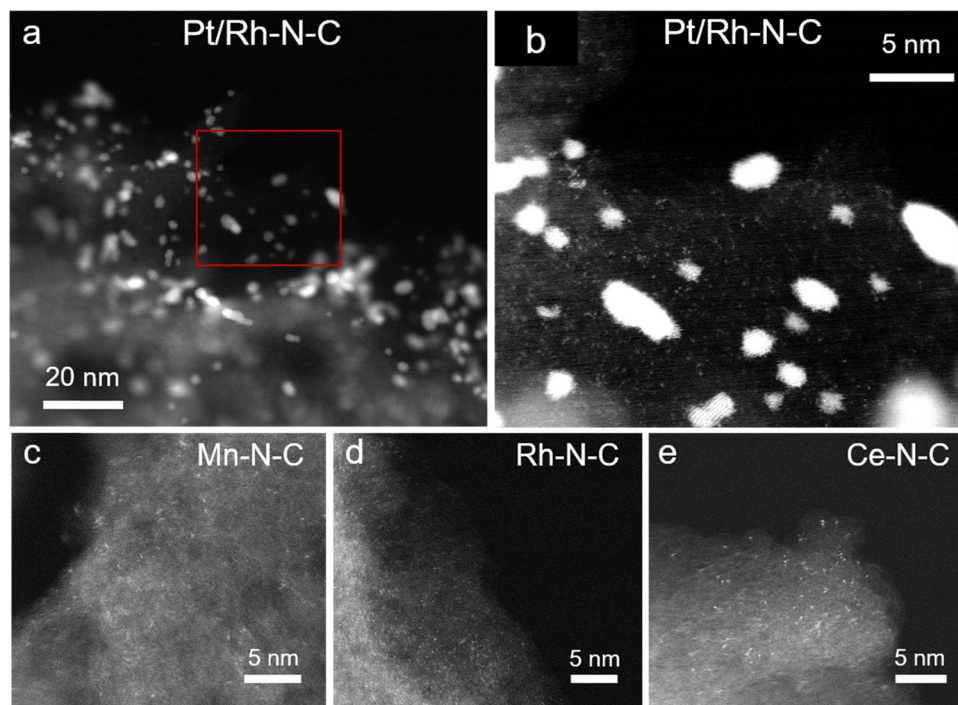
Fig. 2 Representative atomic resolution HAADF-STEM images of a Pt supported on an M−N−C catalyst and representative M−N−C supports. (a) Low magnification image of Pt/Rh−N−C. (b) High magnification image of Pt/Rh−N−C, where the coexistence of Rh single atoms and Pt nanoparticles can be observed. Representative images of a 3d, 4d and f metal M−N−C support (c) Mn−N−C, (d) Rh−N−C and (e) Ce−N−C, where high contrast points indicate atomically dispersed metal sites (see other M−N−C images in ref. 29).
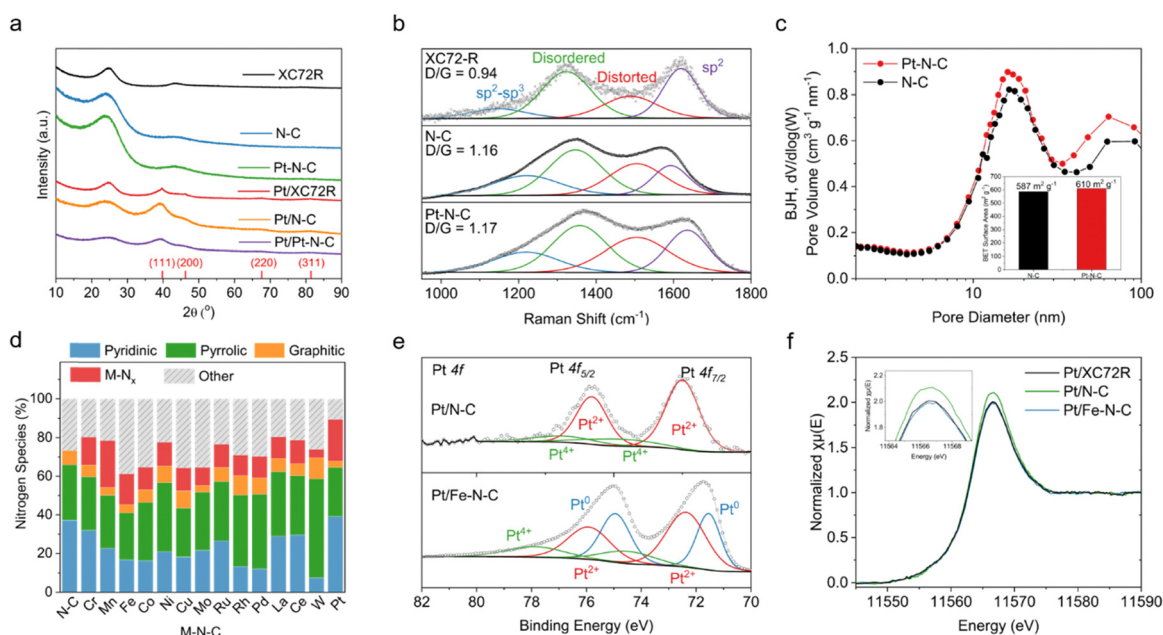

Fig. 3 Physical characterization of the atomically dispersed M−N−C supports. (a) XRD patterns of the catalyst supports and Pt nanoparticles on XC72R and Pt−N−C. (b) Raman spectra of the catalyst supports, XC72R, N−C and Pt−N−C. (c) BJH pore size distribution of the representative M−N−C catalysts. Surface area of the catalysts determined from nitrogen physisorption is given in the inset. (d) N-moiety content from the N 1s XPS spectra. Other species indicate amine, imine, quaternary and NO species. Deconvoluted XPS spectra taken from our recent work.[29] (e) Comparison of the Pt 4f spectra of Pt/N−C and Pt/Fe−N−C (f) Pt L$_3$-edge XANES spectra for Pt/XC72R, Pt/N−C and Pt/Fe−N−C.

M−N−C supports, derived from a deconvoluted high resolution N 1s spectra, as shown for Pt−N−C (and metal free N−C) in Fig.

S4 (ESI†) (data for other M−N−Cs was utilized from our recent study[29]). From Fig. 3d, it is observed that generally, the

concentration of pyridinic and pyrrolic nitrogen is similar between 20–40 at% and 20–35 at%, respectively for all M–N–C's, with the exception of Rh–, Pd– and W–N–C, where a reduced pyridinic (*ca.* 10–15 at%) and increased pyrrolic content (*ca.* 35–50 at%) is observed. The concentration of graphitic and M–N$_x$ species displays only a slight variability between the M–N–C's ranging from 5–10 at% and 10–20 at%, respectively. Despite these ranges in the concentration of N-moieties, no clear trend was observed between any specific N-moiety and its ORR performance (likely due to its supporting nature towards the Pt nanoparticles, rather than the ORR performance of the M–N–C). Fig. S4 (ESI†) shows a typical deconvoluted high resolution N 1s spectrum, containing imine, pyridinic, M–N$_x$, pyrrolic, quaternary, graphitic and NO, N-moieties. The pyridinic, M–N$_x$, pyrrolic and graphitic are the ORR-relevant N-moieties and have been suggested to play a role in ORR activity in the literature. XPS of the Pt 4f region in Fig. 3e elucidates the particle–support interactions of Pt/N–C and Pt/Fe–N–C catalysts. A clear shift towards lower binding energy is observed on the Pt/Fe–N–C catalyst as compared to Pt/N–C, demonstrating the electron donating ability of the Fe–N$_x$ sites to the Pt nanoparticles, a feature that has been previously observed in the literature.[14,18,30]

To further investigate the electronic interaction of the M–N$_x$ sites of the M–N–C support on the chemical state of the Pt nanoparticles, laboratory-based X-ray absorbance (XAS) was performed on an Easy-XAFS spectrometer to evaluate shifts in the X-ray absorption near edge spectroscopy (XANES) Pt L$_3$-edge (11 564 eV). Fig. 3f shows the XANES spectra for the Pt/XC72R standard, Pt/N–C and Pt/Fe–N–C catalysts, where a shift in the white line intensity is observed between the Pt/N–C and Pt/Fe–N–C sample. It has been shown that a decrease in the white line intensity suggests a reduced Pt oxidation state.[31,32] Clearly there is a unique interaction between the Pt nanoparticles and the M–N$_x$ site that is different from the metal free N-moieties. It has been previously hypothesized that when Pt nanoparticles are supported on atomically dispersed M–N$_x$ sites, the increased electronegativity of the Pt nanoparticles acts to draw electrons from the M–N$_x$ sites, in this case Fe–N$_x$.[5,14,18,30] As the Fe–N$_x$ sites donate electrons, the oxidation state of the Pt is reduced, altering its intrinsic catalytic activity, and perhaps increasing its binding strength with the supporting M–N–C. These electron donating interactions are in direct agreement with the Pt 4f XPS spectra, shifting towards lower binding energy for the Pt/Fe–N–C catalyst. The reduced Pt oxidation state on XC72R is perhaps to be due to the increased surface amorphous (sp^3) carbon, resulting from the desulfurization processing, which can act as an electron donor to the Pt nanoparticles.

Therefore, for the ORR analysis, we have successfully synthesized a set of 14 active particle-active support Pt/M–N–C catalysts (and Pt on metal free N–C, Pt/N–C), maintaining the integrity of the atomically dispersed M–N$_x$ site after deposition and demonstrated its chemical interaction with the Pt nanoparticles. It should be noted that representative characterization for the Pt–N–C support is provided in this work, completed characterization of the library of M–N–C materials employed in

this work is provided in our previous work, utilizing AC-STEM/ EDS, single atom electron energy loss spectroscopy (EELS), and XAS, including extended X-ray absorption fine structure (EXAFS) and XANES, XPS, ICP-MS, BET, XRD and Raman to confirm the atomic dispersion, nitrogen coordination and chemical state of the M–N$_x$ sites, as well as the physical properties of the M–N–C materials.[29]

ORR performance of M–N–C and Pt supported on M–N–C

To systematically evaluate the ORR performance of the M–N–C materials and Pt/M–N–C systems, electrochemical measurements were performed in 0.1 M HClO$_4$ using a rotating disk electrode (RDE) configuration. ORR activities were probed by recording the current response on the disk in an O$_2$-saturated LSV (sweeping from 0.05 to 1.05 V *vs.* RHE) at 5 mV s^{-1} and a rotation speed of 1600 rpm as shown in Fig. 4 (all LSVs shown grouped by 3d, 4d and 5d/f metals, for each M–N–C and Pt/M–N–C in Fig. S5–S7, ESI†). Note that all potentials in this work are reported against the reversible hydrogen electrode, RHE. The first column in Fig. 4, comprising Fig. 4a, d and g, shows the LSV for the M–N–C materials, separated by 3d metals (Fig. 4a), 4d metals (Fig. 4b) and 5d/f metals (Fig. 4g). Immediately it is obvious that the metal free N–C has extremely limited ORR performance, having a half-wave potential ($E_{1/2}$) of 0.34 V, consistent with previous reports. For 3d metals, Mn–, Ni– and Cu–N–C exhibit poor ORR performance with delayed ORR onset potentials and $E_{1/2}$ of 0.60, 0.45 and 0.54 V, respectively. Cr– and Co–N–C exhibit increased ORR performance with $E_{1/2}$ of 0.69 and 0.67 V, respectively. Fe–N–C demonstrates the highest ORR performance of the 3d metals, displaying the highest ORR onset potential and $E_{1/2}$ of 0.74 V and a non-negligible kinetic current density (J_K@0.8 V), consistent with previous literature, as Fe–N–C is the most highly studied M–N–C for the ORR.[10,11] For the 4d metals, Mo– and Pd–N–C show poor ORR performance, having delayed ORR onset potentials and $E_{1/2}$ of 0.36 and 0.47 V, respectively. Interestingly, although Ru–N–C has a poor $E_{1/2}$ (0.63 V), the ORR onset potential and J_K (@0.8 V) are more favorable than Fe– and Rh–N–C (the top performing M–N–Cs for the ORR). Rh–N–C is not only the top performing 4d metal, but also the highest performing M–N–C in terms of $E_{1/2}$ (0.76 V); however, it exhibits reduced J_K (@0.8 V) compared to Fe–N–C (with similar transport limited current density, J_L). Finally, the 5d and f metals display almost no increased ORR activity over the metal free N–C sample, with Pt–N–C having the lowest $E_{1/2}$ of 0.38 V (despite having the highest concentration of the M–N$_x$ moiety of all M–N–Cs, Fig. 3e), compared to W–N–C (0.39 V), La–N–C (0.40 V) and Ce–N–C (0.41 V).

The second column of Fig. 4, comprised of Fig. 4d, e and h, shows the LSVs for Pt nanoparticles supported on the M–N–Cs, Pt/M–N–C catalysts and reference Pt/C (Sigma 20 wt%), again separated by 3d (Fig. 4d), 4d (Fig. 4e), 5d/f (Fig. 4h) metals. First, it is apparent that the ORR activity is dominated by the Pt nanoparticles as seen by a much narrower spread in the $E_{1/2}$, J_L and J_K, which is expected due to the Pt precursor loading of 20 wt%, in contrast to the low metal loading in the M–N–C supports (often sub 1 wt%). For Pt supported on 3d metal
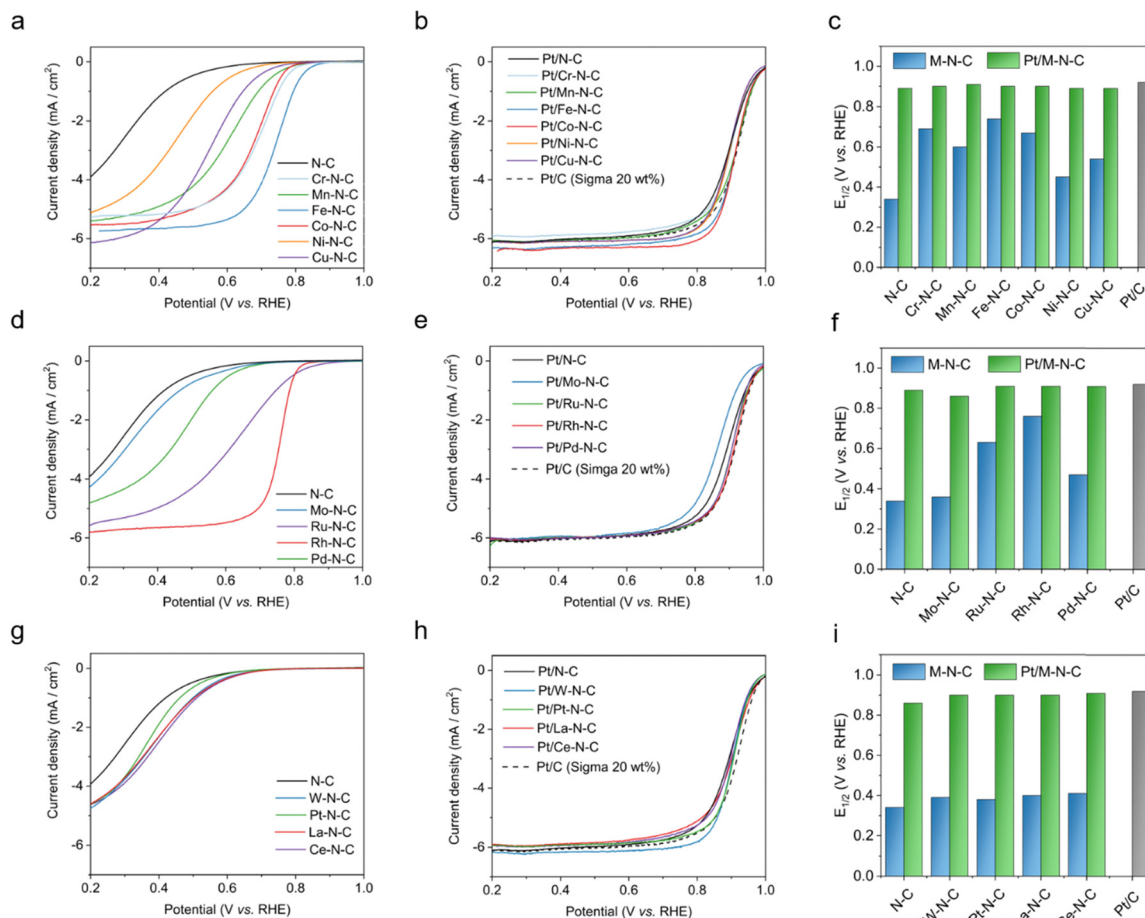
Fig. 4 ORR performance evaluated by RDE in 0.1 M HClO$_4$ with a scan speed of 5 mV s^{-1}. (a)–(c) Half-wave potentials for bare M–N–C catalysts, Pt supported M–N–C (Pt/M–N–C) and summary of half-wave potentials for 3d metals. (d)–(f) Half-wave potential for 4d metals. (g)–(i) Half-wave potentials for 5d and f metals.
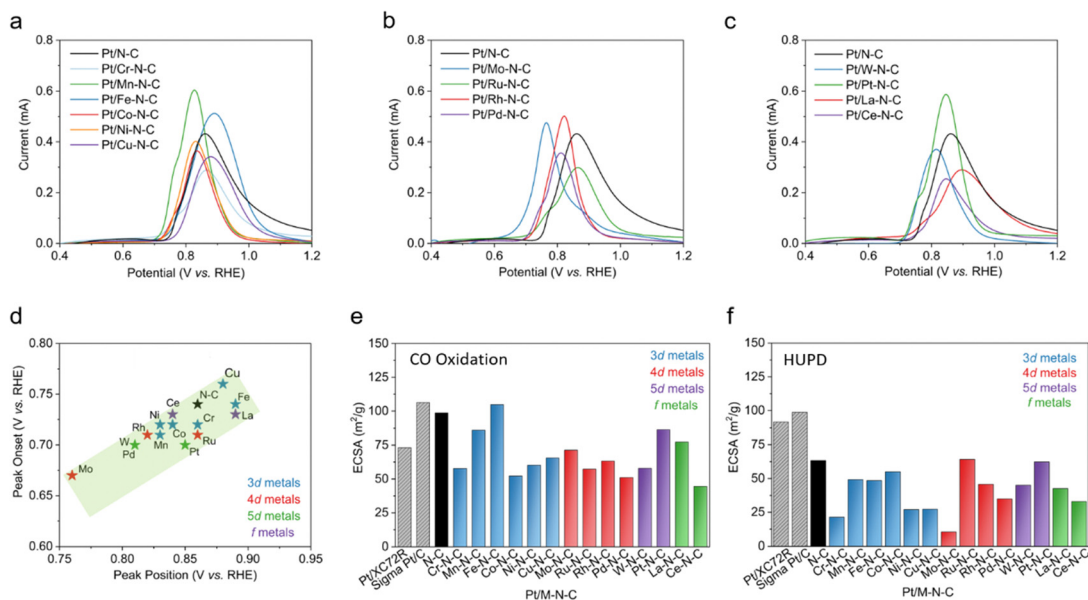

Fig. 5 Carbon monoxide oxidation and ECSA. (a)–(c) CO oxidation peaks for Pt supported on M–N–C's (Pt/M–N–C) for 3d, 4d, 5d and f metals. CO oxidation CV scans were run at 20 mV s^{-1} from 0.1 to 1.23 V vs. RHE. (d) CO oxidation peak onset potential vs. peak position (at maximum intensity). (e) ECSA determined from CO oxidation. (f) ECSA determined from HUPD.

M–N–Cs, the $E_{1/2}$ shifts to 0.9–0.91 V. For Pt on the 4d metal supports, the $E_{1/2}$ is shifted to *ca.* 0.91 V, however, Pt/Mo–N–C shows the lowest $E_{1/2}$ and reduced J_K. The reduced ORR performance of the Mo–N–C and Pt/Mo–N–C could arise due to its highly oxyphilic nature and largest metal content (by ICP-MS).[29] This value is more than double any other M–N–C, causing unfavorable interactions with the Pt nanoparticles, while also interfering with the $4e^-$ ORR pathway. It was recently shown that highly oxyphilic M–N$_x$ sites (*e.g.* Mo–N$_x$) could simultaneously adsorb two oxygen species (*O*O–M–N$_4$), allowing one of the *O to be easily reduced; however, the *O–Mo–N$_4$ site has a high energy barrier for subsequent protonation and reduction of the *O, possibly limiting its ORR performance.[28] For Pt supported on the 5d/f metals, the $E_{1/2}$ of all Pt/M–N–C is shifted to 0.9–0.91 V, with no reduced performance being observed for these highly oxyphilic M–N$_x$ sites, of which all have low metal loadings, highlighting the possible complex relationship between the metal loading of the M–N–C and its impact on the particle–support interactions.[29] The third column of Fig. 4, comprised of Fig. 4c, f and i, summarizes the ORR performance in terms of $E_{1/2}$ for the M–N–C materials and Pt/M–N–C catalyst systems, separated by 3d metal (Fig. 4c), 4d metal (Fig. 4f) and 5d/f metal (Fig. 4i) supports.

Rotating ring disk electrode (RRDE) measurements were conducted to evaluate the peroxide yield (H$_2$O$_2$%) in each of the M–N–C supports and Pt/M–N–C catalysts systems as shown in Fig. S8 (ESI†). All ring currents recorded during the ORR measurements are individually plotted for each M–N–C and Pt/M–N–C are given in Fig. S9–S11 (ESI†). While H$_2$O$_2$ yields vary significantly from 3–26%, no clear trend is observed throughout the selected elements. However, the late 4d and 5d/f elements show high H$_2$O$_2$ yields between 17–25%. Additionally, the M–N–C's which show high H$_2$O$_2$ yields generally have reduced J_L (*e.g.*, Ni–, Mo–, Pd–, W–, Pt–, La– and Ce–N–C). For the Pt/M–N–C catalyst systems, the range of H$_2$O$_2$ yields is largely suppressed, constrained between 1–3%. Demonstrating the strong ability of the Pt nanoparticles to act as scavengers to the corrosive peroxide by-product, enabling the synthesis of ultra-low Pt loading on M–N–C systems to act as peroxide scavengers.

To probe possible interactions between the M–N–C support and Pt nanoparticles, and as a complementary technique to determine the electrochemically active surface area (ECSA), CO stripping experiments were performed between 0.1–1.23 V. Fig. 5a–c shows baseline corrected CO oxidation peaks from the CO stripping experiments for the Pt/M–N–C catalysts separated by 3d metals (Fig. 5a), 4d metals (Fig. 5b) and 5d/f metals (Fig. 5c). In CO oxidation experiments, it is assumed that the underlying M–N–C support is inactive. Furthermore, the Pt nanoparticles come from the same batch and follow the same loading during Pt/M–N–C synthesis. Therefore, changes in the CO oxidation peaks are largely attributed to modifications in the electronic structure of the Pt nanoparticles because of interactions with the M–N–C support. From Fig. 5a–c a range of interesting variations are observed in the shape (narrow/broad) and position of the CO oxidation peak over the varying

M–N–C supports. Fig. 5d plots the potential at the peak maximum against the peak onset potential. Peak onset is a function of the activity of the active site towards CO oxidation and not dependent on fluctuations in Pt loading that are unavoidable during synthesis, and the potential at the peak maximum is again independent from these fluctuations as the numerical value of the current is not considered in this plot. From Fig. 5d, the only clear outlier is Pt/Mo–N–C, having a clearly reduced onset potential and peak position. This more drastic reduction in CO oxidation potential could result from the significantly larger metal loading in the Mo–N–C (*ca.* 5 wt%), having a larger impact on the chemical state of the Pt nanoparticles. There is no clearly observable trend among the other M–N–Cs, having a peak maximum potential between 0.81–0.88 V and a peak onset of 0.70–0.76 V, regardless of the class of the M–N$_x$ site (3d, 4d, 5d/f metal). Therefore, suggesting that the general CO oxidation mechanism remains the same over the Pt/M–N–C catalysts, with peak broadening or slight shifts in the onset potential arising from interactions between the Pt nanoparticles and M–N–C support. CO oxidation peaks for the reference Pt/XC72R and Sigma (20 wt%) Pt/C catalysts are shown in Fig. S12 (ESI†), where a peak maximum is observed at *ca.* 0.85 V and an onset potential of *ca.* 0.70 V. Interestingly, the in house Pt/XC72R catalyst shows a peak shoulder at 0.75 V, which is also observed for several Pt/M–N–Cs (M = Mn, Cr, Ru, Pd, Pt and La), where a clear shoulder at a lower potential is observed, suggesting the presence of active sites where CO is more easily oxidized on the Pt nanoparticle. While the exact potential at which the shoulder is located shifts with different M–N$_x$ centers, this feature is likely attributed to the morphology of the in-house Pt nano-particles. These interactions with the M–N$_x$ site can alter the electronic structure of the Pt nanoparticles, creating sites that either promote or inhibit CO oxidation performance and enabling catalyst tailorability. The ECSA for each Pt/M–N–C system was determined by integrating the CO oxidation peak and converting to surface area by a conversion factor of 420 μC cm^{-2}. Fig. 5e shows the ECSA determined through CO oxidation, where Pt/Fe–N–C has the highest ECSA (104.8 m^2 g^{-1}), while the majority of the Pt/M–N–C catalysts have ECSAs between *ca.* 50–70 m^2 g^{-1}. Additionally, hydrogen-underpotential deposition (HUPD) from the CV (Fig. S13–S15, ESI†) was also used to determine ECSA, as shown in Fig. 5f, which yields a smaller ECSA compared to that determined through CO oxidation, which is expected as CO oxidation tends to overestimate, while HUPD underestimates the ECSA.[33] HUPD is known to underestimate the ECSA of Pt catalyst, especially Pt alloys or when the electronic structure of the Pt has been modified. In this work, it is possible that the interactions with the M–N$_x$ sites alters the Pt electronic structure, affecting the adsorption energy of the H atoms, leading to further under-estimation of the ECSA through HUPD. Where in the case of Mo–N$_x$, the Mo loading is significantly higher than the other M–N–Cs (*ca.* 5 wt%), leading to more electronic interactions with the Pt nanoparticles, perhaps resulting in the lowest ECSA being observed through the HUPD technique (12.5 m^2 g^{-1}).[33,34] Most of the Pt/M–N–C catalysts show an ECSA$_{HUPD}$ between *ca.* 20–55 m^2 g^{-1}, lower than the standard Pt/C of 106 m^2 g^{-1}.

Interestingly, during the CV, the Pt/Mo–N–C exhibits an additional peak in both anodic and cathodic sweep (at *ca.* 0.3 V to 0.8 V), which was not observed in the Mo–N–C sample (without Pt nanoparticles), but has been previously observed in Pt–Mo catalysts and attributed to redox transitions of the Mo from the Mo^{4+} to Mo^{6+} state, further evidencing a change in the chemical nature of the Pt nanoparticles due to interactions with the Mo–N_x sites.[35–38]

ORR activities

To evaluate the performance of the Pt/M–N–C systems, the mass activities (M_A) and specific activities (S_A) utilizing the ECSA$_{HUPD}$, were calculated as shown in Fig. 6. The M_A is calculated *via* the kinetic current calculated by the Koutecky–Levich equation and the Pt mass loading on the working electrode, demonstrating the catalytic ability of the Pt per unit mass. From Fig. 6a, Pt supported by several 3d metal supports (Mn–, Fe– and Co–N–C) achieve a competitive M_A of *ca.* 220 A g_{Pt}^{-1}, with Pt/Co–N–C achieving the highest M_A of 235 A g_{Pt}^{-1}. For the 4d, 5d and f metal supports, only Pt/Rh–N–C achieves a similar M_A of 230 A g_{Pt}^{-1}. These catalysts outcompete the in-house 20 wt% Pt/XC72R (209.5 A g_{Pt}^{-1}) and are competitive with a 20 wt% Pt/C Sigma-Aldrich standard (291.5 A g_{Pt}^{-1}). The S_A reveals the intrinsic catalytic activity of the Pt per unit area. Interestingly, although the Pt/M–N–C catalysts display a modest M_A compared to the Pt standards, the S_A is significantly enhanced. The intrinsic activity of the Pt nanoparticles is significantly enhanced, possibly due to the interactions of the M–N–C support over a typical XC72R carbon support. From Fig. 6b although the Pt/N–C system shows a reduced S_A compared to the Pt/XC72R (256 μA cm^{-2}) and 20 wt% Pt Sigma-Aldrich Pt/C (295 μA cm^{-2}) standards, the introduction of a metal to the M–N–C, improving the particle–support interactions, yields improved S_A, regardless of the M–N_x site utilized in this work. Pt/Cr–N–C demonstrates the largest S_A (*ca.* 670 μA cm^{-2}) and improvement of nearly 2–3× over the reference Pt/C catalysts. In general, the S_A for Pt/M–N–C is quite high in the range of *ca.* 400–600 μA cm^{-2}. S_A based on the ECSA$_{CO-Oxidation}$ are given in Fig. S16 (ESI†), where again the Pt/M–N–Cs display an increased S_A over the Pt/C standards, with Pt/Co–N–C displaying the highest S_A (ECSA$_{CO-Oxidation}$) of *ca.* 460 μA cm^{-2}. Although it's been shown previously that a higher Pt loading

typically lead to higher activities (when normalized to total Pt weight), the target loading of this work was 10–20 wt% Pt to prevent the total activity being dominated by the Pt at ultra-high loadings (>40 wt%), while also preventing the deactivation of Pt at ultra-low loadings (<5 wt%). Ultimately, in this work, the active M–N–C support enhances the intrinsic catalytic activity of the Pt nanoparticles (over the reference materials), as evidenced by its high S_A. Although its reduced ECSA indicates fewer accessible active sites, limiting its M_A. The sites that are accessible possess increased ORR activity, therefore the ECSA for the Pt/M–N–C catalyst, a parameter which could be further optimized by tailoring synthesis parameters, must be enhanced.

Catalyst durability under load-cycling and start-up/shut-down protocols

The supporting carbon-based material is known to significantly impact the catalyst durability, influenced by its physical and chemical properties (*i.e.*, carbon porosity, surface chemistry, and degree of graphitization). Previous literature has hypothesized that utilizing M–N–C materials as active supports strengthens the nanoparticle–support and ionomer–support interactions.[14,15,39] Although the precise particle–support interactions have not yet been elucidated, the atomically dispersed M–N_x sites are believed to have strong interactions with the Pt nanoparticles (by altering the electronic structure, increasing catalytic activity and stability within the support) and similarly, the effect of a nitrogen doped support is believed to aid in the anchoring of the ionomer.[39] Both effects may provide better ionomer coverage of the Pt nanoparticles, while possibly decreasing the nanoparticle diffusion and dissolution.

In this work, we evaluated the durability of 5 samples, the Fe–N–C and Rh–N–C samples and the corresponding Pt loaded samples, Pt/Fe–N–C and Pt/Rh–N–C, as well as the standard Pt/C (Sigma-Aldrich). Durability measurements were performed over two potential ranges. First, a more mild drive cycle protocol cycling between 0.6–1.0 V and a second harsher start-up shut-down protocol cycling between 1.0–1.5 V, for up to 10 000 cycles, as shown in Fig. 7a.

In the lower potential range of the drive cycle, the durability of the Pt nanoparticle is impacted more than the carbon-based support (although it should be noted that Pt-assisted carbon
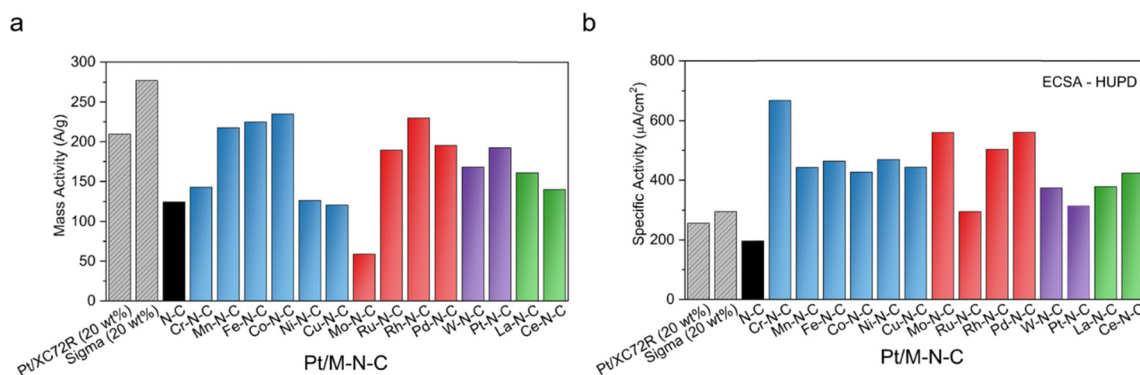

Fig. 6 ORR activity metrics for Pt supported on M–N–C's. (a) Mass activity at 0.9 V *vs.* RHE and (b) specific activity (ECSA from HUPD).
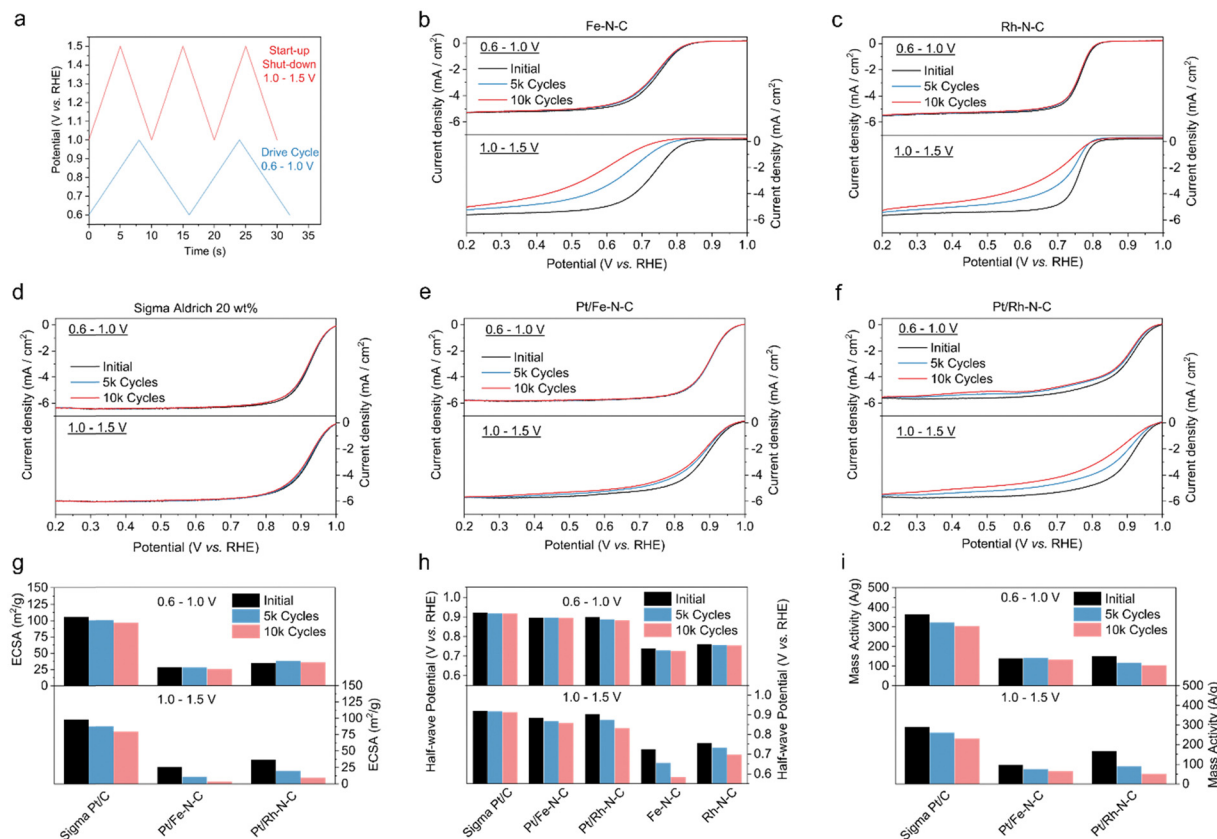
Fig. 7 Catalyst stability tests in an RDE confirmation. (a) Protocols selected for stability testing. Stability testing evaluating half-wave potential of the initial catalyst and after 5k and 10k cycles, of (b) bare Fe–N–C, (c) bare Rh–N–C, (d) Sigma-Aldrich 20 wt% Pt standard, (e) Pt/Fe–N–C and (f) Pt/Rh–N–C. Summary plots of (g) catalyst ECSA (determined through HUPD), (h) half-wave potentials and (i) mass activities. Where the top segment in all figures is for the milder protocol cycling between 0.6 and 1.0 V, while the bottom segment is for the more aggressive protocol cycling between 1.0 and 1.5 V.

oxidation of the amorphous carbon can occur as well). The catalyst LSV performance after 5000 and 10 000 cycles is evaluated and for the drive cycle protocol, is presented in the top section of each graph in the top half of Fig. 7b–f, and summarized in top half of Fig. 7g–i. All five catalysts examined are relatively stable, in terms of $E_{1/2}$ and ECSA, with the Pt/Rh–N–C sample showing a loss of 16 mV after 10k cycles. However, in terms of M_A loss, the Pt/C standard and Pt/Rh–N–C show significant decreases of 16.3% and 31.1%, respectively. On the other hand, the Pt/Fe–N–C catalyst shows an $E_{1/2}$ loss of only 2 mV and a M_A loss of 4.3%, after 10k cycles. This result demonstrates that not all Pt/M–N–C systems display the same durability, while showing the robust nature of the Pt/Fe–N–C catalyst in the 0.6–1.0 V range.

Despite the robust nature of the Pt/M–N–C catalysts in the lower potential range, in the high potential range, simulating a start-up shut-down protocol, more significant degradation to the $E_{1/2}$, M_A and ECSA is observed, as shown in bottom half of Fig. 7b–f, and summarized in bottom half of Fig. 7g–i. This higher potential region of 1.0–1.5 V can be experienced at PEMFC cathodes through current reversal and typically induces degradation to the carbon-based support (carbon corrosion). Significant degradation is observed on the $E_{1/2}$ for the Fe–N–C, Rh–N–C and Pt/Rh–N–C catalysts, showing reductions of

ca. 140 mV, 60 mV and 60 mV, respectively after 10k cycles. Interestingly, for the Pt/Fe–N–C catalyst, only a slight reduction of 26 mV is observed in the $E_{1/2}$ after 10k cycles, suggesting that the interaction between the Fe–N–C and Pt nanoparticles helps maintain the intrinsic catalytic activity of the Pt nanoparticles. Significant losses are observed for both the Pt/Fe–N–C and Pt/Rh–N–C after 10k cycles in terms of M_A, showing reductions of 32.7% and 69.2%, and in terms of ECSA with reductions of 85.6% and 73.1%, respectively. In contrast, the Pt/C standard shows $E_{1/2}$, M_A and ECSA losses of only 8 mV, 20.8% and 19.2%, respectively. These durability results highlight a few main points. First, after 10k of the harsher start-up shut-down cycles, although an almost complete loss of ECSA (3.7 m² g⁻¹ after 10k cycles) is observed for the Pt/Fe–N–C catalyst, the specific activity of the Pt nanoparticles is extremely high (1800 μA cm⁻²) in contrast to the Pt/C standard of (290 μA cm⁻²), after the 10k start-up shut-down cycles, Fig. S17 (ESI†). The issue arises in the stability of the carbon matrix of the Fe–N–C (more generally all of the M–N–Cs) on which the Pt nanoparticles are supported. The more graphitic carbon support of the Pt/C standard (as seen in Fig. 3) presents better durability than the less graphitic (more amorphous) M–N–C supports. This presents a clear target to improve for not only more active Pt based catalysts, but also more durable catalysts, by synthesizing M–N–C based supports with a larger graphic content.

Conclusions

In summary, we have synthesized a library of 14 atomically dispersed M–N–C catalysts, consisting of 3d, 4d, 5d and f metals, as ORR catalysts and active supports for Pt nanoparticles, Pt/M–N–C. Valence state analysis through XANES and XPS demonstrate interactions between the M–N_x site and Pt nanoparticles, where electron donation effects from the M–N_x site, reduce the Pt nanoparticle oxidation state. ORR testing revealed that Fe–N–C and Rh–N–C are the most active M–N–Cs for the ORR. When acting as an active support for the Pt nanoparticles (*ca.* 20 wt%), the intrinsic catalytic activity of the Pt nanoparticles (in terms of S_A) is significantly enhanced compared to the Pt/C standards, with competitive M_A values, particularly for Pt/Fe–N–C and Pt/–Rh–N–C. CO stripping experiments revealed the distinct interactions of the M–N–C supports with the Pt nanoparticles (supported by XANES and XPS), leading to distortions in the CO oxidation peak shape and position. Such interactions could be utilized to not only enhance anchoring of the Pt nanoparticles into the M–N–C matrix, but also tailor more favorable adsorption energies for reaction intermediates. Durability testing revealed the robust nature of the Pt/M–N–C catalysts in the lower potential (0.6–1.0 V) drive cycle protocol, while suffering from degradation in the higher potential (1.0–1.5 V) start-up shut-down protocol. The durability tests revealed the extremely high specific activity of the Pt/Fe–N–C catalyst over the Pt/C standard, but simultaneously highlighted the importance of obtaining a M–N–C support with a higher graphitic content, which can better resist carbon corrosion in the higher potential regimes. This work presents a platform for creating highly active hybrid Pt/M–N–C catalysts, showcasing the variation in activity as one traverses the periodic table, while highlighting important design criteria for highly active and durable catalysts. To fully exploit the enhanced intrinsic catalytic activity of Pt/M–N–C catalysts, future studies leveraging both computation and experiment are required to gain a more fundamental understanding of the chemical interactions of the M–N_x sites and Pt nanoparticles.

Materials and methods

Chemicals

$H_2PtCl_6 \cdot 6(H_2O)$, NaOH, and ethylene glycol were purchased and used as-received from Sigma-Aldrich and Fisher-Scientific. $HClO_4$ was purchased from Sigma-Aldrich and used at the correct dilution (0.1 M). Pure (99.9999% research grade) nitrogen gas, pure (99.9999% research grade) oxygen gas, and 99.5% purity carbon monoxide gas was purchased and used as-received from Praxair. Nicarbazin (Sigma-Aldrich), CAB-O-SIL® LM-150 fumed silica (Cabot), Aerosil® OX-50 (Evonik), iron(III) nitrate nonahydrate (Sigma-Aldrich), chromium(III) acetylacetonate (Sigma-Aldrich), manganese(II) nitrate tetrahydrate (Sigma-Aldrich), cobalt(II) nitrate hexahydrate (Sigma-Aldrich), nickel(II) nitrate hexahydrate (Sigma-Aldrich), copper(II) nitrate hemi pentahydrate (Sigma-Aldrich), ammonium molybdate tetrahydrate (Sigma-Aldrich), ruthenium(III) nitrosylnitrate (Alfa Aesar), rhodium(III) nitrate hydrate (Sigma-Aldrich), palladium(II) nitrate dihydrate (Sigma-Aldrich), lanthanum(III) nitrate hexahydrate (Alfa Aesar), cerium(III) nitrate hexahydrate (Fisher Scientific), ammonium paratungstate (Sigma-Aldrich) and tetraammineplatinum(II) nitrate (Sigma-Aldrich).

Synthesis

Platinum nanoparticles. An aliquot (equivalent to 300 mg of Pt metal content) of the aqueous chloroplatinic acid stock solution was taken and dispersed in ethylene glycol. This solution was further diluted in ethylene glycol to 30 mg of Pt metal content per microwave heating vessel for a total of 10 heating vessels. 1 M NaOH was added dropwise to each vessel and tested for pH until the value reached pH 10. The vessels were sealed and heated in the microwave reactor (CEM MARS 6) with a ramp time of 5 min to 180 °C and held for 20 min. The vessels were allowed to cool to 50 °C before combining all vessel solutions into a single stock flask. Afterwards, the pH of the stock solution was adjusted to pH 3 to prevent further reduction by the dropwise addition of 1 M H_2SO_4.

M–N–C catalysts. The atomically dispersed M–N–C catalysts were synthesized using the robust sacrificial support method (SSM). The general procedure is as follows. First, 6.25 g of nicarbazin, 1.25 g LM-150, 1.25 g OX-50, 0.5 g of Stöber spheres and a determined amount of metal salt precursor are added to 50 mL of water under magnetic stirring. The precursor slurry is then sonicated for 30 min and then dried for 24 hours at 45 °C under constant stirring. The mixture is then fully dried in an oven at 45 °C for another 24 hours. Next, the dried precursor mix is ball milled at 45 Hz for 1 hour. The milled powder is then pyrolyzed for a first time (the conditions are as noted below). Following the first pyrolysis, the catalyst is then ball milled again for 1 hour before being placed in 15 M HF acid solution for 72 hours to remove the silica template. Following the acid wash, the catalyst is centrifuged and filtered until neutral pH and then dried at 45 °C. The now etched catalyst is pyrolyzed for a second time (the conditions are as noted below). Lastly, the catalyst is ball milled a final time for 1 hour.

Synthesis of (Mn–, Fe–, Co–, Ni–, Cu–, Mo– and W–N–C) catalysts. The synthesis of these materials follows the general scheme above, with the first pyrolysis under a reductive H_2/Ar (7%/93%) atmosphere for 45 min at 975 °C (with a ramp rate of 15 °C min^{-1}). The second pyrolysis is again under a reductive NH_3/N_2 (10%/90%) atmosphere for 45 min at 950 °C (ramp rate of 20 °C min^{-1}). The metal salt precursor loadings are Mn = 0.266 g, Fe = 0.60 g, Co = 0.272 g, Ni = 0.271 g, Cu = 0.345 g, Mo = 0.262 g and W = 0.095 g.

Synthesis of Cr–N–C catalyst. The synthesis follows the general procedure mentioned previously, with an adaptation of the pyrolysis conditions to maintain an atomic dispersion of the Cr sites. The first and second pyrolysis temperatures are reduced to 650 °C. The metal salt precursor loading of Cr = 0.519 g.

Synthesis of Ru–N–C and Pt–N–C catalyst. The synthesis follows the general procedure mentioned previously, with an adaptation of the pyrolysis conditions to maintain an atomic dispersion of the Ru sites. The pyrolysis temperatures are reduced to 650 °C and both pyrolysis steps are performed in an inert Ar atmosphere. The metal salt precursor loading of Ru = 0.235 g and Pt = 0.072 g.

Synthesis of Rh and Pd–N–C catalysts. The synthesis follows the general procedure mentioned previously, with an adaptation of the pyrolysis conditions to maintain an atomic dispersion of the Rh and Pd sites. The pyrolysis is performed at the high temperature of 975 °C and 950 °C for the first and second pyrolysis, respectively. However, both pyrolysis steps are performed in an inert Ar atmosphere. The metal salt precursor loadings are Rh = 0.215 g and Pd = 0.198 g.

Synthesis of La and Ce–N–C catalysts. The synthesis follows the general procedure mentioned previously, with an adaptation of the pyrolysis and etching conditions to maintain an atomic dispersion of the La and Ce sites. The pyrolysis temperatures are reduced to 650 °C and both pyrolysis steps are performed in an inert Ar atmosphere. To prevent the formation of LaF_3 and CeF_3, the etching of the silica template is done in a 4 M NaOH environment at 80 °C for 4 days. The metal salt precursor loadings are La = 0.060 g and Ce = 0.061 g.

Pt supported on M–N–C hybrid catalysts. Aliquots of the Pt stock solution were used in the deposition of Pt onto the M–N–C materials by combining the stock solution with the M–N–C materials powder in a 50/50 blend of water/ethylene glycol. The mixture was stirred for 24 hours prior to vacuum filtration and subsequent drying in an oven at 60 °C. The resulting powder was ground using an agate pestle and mortar and used as prepared for materials characterizations and catalyst ink preparation. The Pt amount was adjusted to achieve a *ca.* 20 wt% Pt loading on the M–N–C, N–C and XC72R supports.

Materials characterizations

X-ray diffraction (XRD). Powder XRD patterns were taken on a Rigaku Ultima III X-ray diffractometer using a scan speed of $2°$ min^{-1} from $5°$ to $90°$. The XRD wavelength was 1.5404 Å.

Scanning electron microscopy (SEM). SEM micrographs were taken on an FEI Magellan 400 XHR SEM microscope with an accelerating voltage of 20 kV and emission current of 50 pA.

Aberration-corrected scanning transmission electron microscopy (AC-STEM). AC-STEM images and energy dispersive X-ray spectroscopy (EDS) elemental maps were obtained used a JEOL ARM300CF microscope at an acerating voltage of 300 kV.

X-ray photoelectron spectroscopy (XPS). XPS spectra were taken using a Kratos AXIS Supra spectrometer with a monochromatic Al K-alpha source. All XPS data was fit using the CasaXPS software. A 70% Gaussian/30% Lorentzian parameter was set for the fittings.

Raman spectroscopy. The Raman spectra were obtained on a Horiba LabRAM HR Evolution confocal Raman microscope with 633 nm laser and 600 g mm^{-1} grating. 100× objective was applied. Ten individual 20 s spectra were accumulated. CasaXPS software was used to do the fitting based on the previous publications.

Brunauer–Emmett–Teller (BET) analysis. A Micromeritics 3Flex Analyzer at 77 K was used to obtain the N_2 physisorption measurements, utilizing a low-pressure dose mode (5 cm^3 g^{-1}). The Brunauer–Emmett–Teller (BET) method and Barret–Joyner–Halenda model (BJH) were used to quantify the surface area and pore size distribution, respectively.

Inductively coupled plasma-mass spectrometry (ICP-MS). To accurately quantify the low metal content in the atomically dispersed M–N–C supports, ICP-MS was performed using an Aligent 5510 system.

Electrochemical characterizations. All electrochemical characterization was completed in glassware made by Adams & Chittenden in 0.1 M $HClO_4$ aqueous electrolyte. The working electrode (WE) used was a PTFE separated and lined glassy carbon disc with platinum ring. The counter electrode (CE) used was a carbon rod and the reference electrode (RE) used was an RHE (Gaskatel). Tests were completed using a Pine Research rotator and either Bio-Logic or Gamry potentiostats. Catalyst inks were air-dried after deposition onto the glassy carbon portion of the working electrodes with loadings of 360 μg cm^{-2} for M–N–C materials and 40 μg$_{Pt}$ cm^{-2} for the hybrid Pt/M–N–C catalysts.

Oxygen reduction reaction activity. Pure nitrogen gas was purged for 600 s prior to the start of all electrochemical tests. The working electrode was then submerged in the electrolyte without rotation and the EIS, activation CVs (500 mV s^{-1} from 0.1 V to 1.23 V), and slow scan CVs (20 mV s^{-1} from 0.1 V to 1.23 V) were recorded. The rotation speed was changed to 1600 rpm and the working electrode disc and ring LSVs were recorded (5 mV s^{-1} from 0.05 V to 1.05 V). Then the electrolyte was bubbled with pure oxygen gas for 300 s before recording the disc and ring LSVs in the same window and scan speeds. ECSA from hydrogen underpotential deposition was determined from the CV scans under a N_2 atmosphere with no rotation. The CV curves were integrated between 0.05–0.40 V *vs.* RHE (where the current density reaches the capacitive current steady state). The ECSA was determined using eqn (1).

$$ECSA,\ m^2\ g^{-1}$$
$$= \frac{(H_{desorption}\text{peak area, A V})}{(210\ \mu C\ cm_{Pt}^{-2})(\text{scan rate, V s}^{-1})(\text{total Pt mass, g})} \quad (1)$$

Oxygen reduction reaction stability. Stability of the catalyst samples was checked by comparing the activities from the CVs and LSVs at 0 cycles (fresh), 5000 cycles (half-aged), and 10 000 cycles (fully aged) in two potential ranges at room temperature (25 °C). At each stage, the N_2 CVs, N_2 LSVs, and O_2 LSVs were recorded as referenced in the previous section for ORR activity. The first potential cycling range was defined as the load-cycling or operational protocol in which the working electrode was cycled from 0.6 V to 1.0 V at 50 mV s^{-1}.

The second potential cycling range was defined at the start-up and shut-down protocol in which the working electrode was cycled from 1.0 V to 1.5 V at 100 mV s^{-1}.

Carbon monoxide oxidation. Catalysts first underwent an initial 100 cycles of activation CVs (500 mV s^{-1} from 0.1 V to 1.23 V). The CO gas was then introduced to the electrolyte by light bubbling while applying 0.1 V to the WE for 180 s. The electrolyte was then purged for 600 s with pure nitrogen gas to remove excess CO gas. CVs were then run for 3 cycles (20 mV s^{-1} from 0.1 V to 1.23 V) to obtain the CO stripping curve and the subsequent N$_2$ CV curve.

Hydrogen peroxide yield and collection efficiency. The total peroxide yield ($X_{H_2O_2}$) was collected by RRDE and calculated using the ring current (I_{ring}), disc current (I_{disc}), and collection efficiency (C.E.) of the working electrode by eqn (2):[40–42]

$$X_{H_2O_2} = \frac{(2 \times I_{ring})/C.E.}{I_{disc} + \left(I_{ring}/C.E.\right)} \times 100\ \%$$ (2)

The collection efficiency was separately determined by RRDE using a ferri/ferro-cyanide redox couple and calculated simply using the measured ring and disc limiting current values (eqn (3)):

$$C.E. = -\frac{I_{ring}}{I_{disc}}$$ (3)

Briefly, the collection efficiency experiments were set up by using the RRDE working electrode tip deposited with either Fe–N–C or Pt/Fe–N–C as the standardized catalysts and a deaerated electrolyte of 0.1 M NaOH with 10 mM K$_3$Fe(CN)$_6$ (a standard compound used for this purpose). The potential is swept from 0.2 V to 1.6 V $vs.$ RHE at 5 mV s^{-1} and the efficiency is calculated at 0.4 V $vs.$ RHE. During this linear sweep voltammetry, [Fe(CN)$_6$]$^{4-}$ is produced at the disk electrode which is oxidized to [Fe(CN)$_6$]$^{3-}$ at the ring electrode with insignificant contributions from other reactions. For added accuracy, these experiments were performed on both catalyst samples (Fe–N–C and Pt/Fe–N–C) on two different RRDE working electrodes and the rotation speed of 100 rpm was used for the calculation purposes (due to the curve reaching a constant, well defined limiting current for both the disk and the ring).

Conflicts of interest

The authors declare no competing financial interest.

Acknowledgements

References

1 W. Xia, A. Mahmood, Z. Liang, R. Zou and S. Guo, Earth-Abundant Nanomaterials for Oxygen Reduction, *Angew. Chem., Int. Ed.*, 2016, **55**(8), 2650–2676, DOI: **10.1002/anie.201504830**.

2 J. Greeley, I. E. L. Stephens, A. S. Bondarenko, T. P. Johansson, H. A. Hansen, T. F. Jaramillo, J. Rossmeisl, I. Chorkendorff and J. K. Nørskov, Alloys of Platinum and Early Transition Metals as Oxygen Reduction Electrocatalysts, *Nat. Chem.*, 2009, **1**(7), 552–556, DOI: **10.1038/nchem.367**.

3 A. Ly, T. Asset and P. Atanassov, Integrating Nanostructured Pt-Based Electrocatalysts in Proton Exchange Membrane Fuel Cells, *J. Power Sources*, 2020, **478**(August), 228516, DOI: **10.1016/j.jpowsour.2020.228516**.

4 M. Lefèvre, E. Proietti, F. Jaouen and J. P. Dodelet, Iron-Based Catalysts with Improved Oxygen Reduction Activity in Polymer Electrolyte Fuel Cells, *Science*, 2009, **324**(5923), 71–74, DOI: **10.1126/science.1170051**.

5 X. Yang, C. Priest, Y. Hou and G. Wu, Atomically Dispersed Dual-metal-site PGM-free Electrocatalysts for Oxygen Reduction Reaction: Opportunities and Challenges, *SusMat*, 2022, **2**(5), 569–590, DOI: **10.1002/sus2.69**.

6 S. Rojas-Carbonell, C. Santoro, A. Serov and P. Atanassov, Transition Metal–Nitrogen–Carbon Catalysts for Oxygen Reduction Reaction in Neutral Electrolyte, *Electrochem. Commun.*, 2017, **75**, 38–42, DOI: **10.1016/j.elecom.2016.12.011**.

7 Z. Jin, P. Li, Y. Meng, Z. Fang, D. Xiao and G. Yu, Understanding the Inter-Site Distance Effect in Single-Atom Catalysts for Oxygen Electroreduction, *Nat. Catal.*, 2021, **4**(7), 615–622, DOI: **10.1038/s41929-021-00650-w**.

8 S. Liu, C. Li, M. J. Zachman, Y. Zeng, H. Yu, B. Li, M. Wang, J. Braaten, J. Liu, H. M. M. Iii, M. Lucero, A. J. Kropf, E. E. Alp, Q. Gong, Q. Shi, Z. Feng, H. Xu, G. Wang, D. J. Myers, J. Xie, D. A. Cullen and S. Litster, Atomically Dispersed Iron Sites with a Nitrogen–Carbon Coating as Highly Active and Durable Oxygen Reduction Catalysts for Fuel Cells, *Nat. Energy*, 2022, **7**, 652–663, DOI: **10.1038/s41560-022-01062-1**.

9 L. Jiao, J. Li, L. L. R. Richard, Q. Sun, T. Stracensky, E. Liu, M. T. Sougrati, Z. Zhao, F. Yang, S. Zhong, H. Xu, S. Mukerjee, Y. Huang, D. A. Cullen, J. H. Park, M. Ferrandon, D. J. Myers, F. Jaouen and Q. Jia, Chemical Vapour Deposition of Fe–N–C Oxygen Reduction Catalysts with Full Utilization of Dense Fe–N$_4$ Sites, *Nat. Mater.*, 2021, **20**(10), 1385–1391, DOI: **10.1038/s41563-021-01030-2**.

10 T. Asset and P. Atanassov, Iron-Nitrogen-Carbon Catalysts for Proton Exchange Membrane Fuel Cells, *Joule*, 2020, **4**(1), 33–44, DOI: **10.1016/j.joule.2019.12.002**.

11 X. Zhang, L. Truong-phuoc, T. Asset, S. Pronkin and C. Pham-huu, Are Fe–N–C Electrocatalysts an Alternative to Pt-Based Electrocatalysts for the Next Generation of Proton Exchange Membrane Fuel Cells?, *ACS Catal.*, 2022, **12**(22), 13853–13875, DOI: **10.1021/acscatal.2c02146**.

12 S. Zaman, Y. Su, C. Dong, R. Qi, L. Huang, Y. Qin, Y. Huang, F. Li, B. You, W. Guo, Q. Li, S. Ding and B. Yu Xia, Scalable Molten Salt Synthesis of Platinum Alloys Planted in Metal–Nitrogen–Graphene for Efficient Oxygen Reduction, *Angew. Chem., Int. Ed.*, 2022, **61**(6), e202115835, DOI: **10.1002/ange.202115835**.

13 L. Huang, Y. Q. Su, R. Qi, D. Dang, Y. Qin, S. Xi, S. Zaman, B. You, S. Ding and B. Y. Xia, Boosting Oxygen Reduction via Integrated Construction and Synergistic Catalysis of Porous Platinum Alloy and Defective Graphitic Carbon, *Angew. Chem., Int. Ed.*, 2021, **60**(48), 25530–25537, DOI: **10.1002/anie.202111426**.

14 Z. Qiao, C. Wang, C. Li, Y. Zeng, S. Hwang, B. Li, S. Karakalos, J. Park, A. J. Kropf, E. C. Wegener, Q. Gong, H. Xu, G. Wang, D. J. Myers, J. Xie, J. S. Spendelow and G. Wu, Atomically Dispersed Single Iron Sites for Promoting Pt and Pt3Co Fuel Cell Catalysts: Performance and Durability Improvements, *Energy Environ. Sci.*, 2021, **14**(9), 4948–4960, DOI: **10.1039/d1ee01675j**.

15 L. Liang, H. jin, H. Zhou, B. Liu, C. Hu, D. Chen, J. Zhu, Z. Wang, H. W. Li, S. Liu, D. He and S. Mu, Ultra-Small Platinum Nanoparticles Segregated by Nickle Sites for Efficient ORR and HER Processes, *J. Energy Chem.*, 2021, **65**, 48–54, DOI: **10.1016/j.jechem.2021.05.033**.

16 Q. Feng, X. Wang, M. Klingenhof, M. Heggen and P. Strasser, Low-Pt NiNC-Supported PtNi Nanoalloy Oxygen Reduction Reaction Electrocatalysts—In Situ Tracking of the Atomic Alloying Process, *Angew. Chem., Int. Ed.*, 2022, **61**(36), DOI: **10.1002/anie.202203728**.

17 X. Wang, Y. Li, C. Yang, J. Lu, L. Cao and H. P. Liang, Surfactant-Assisted Implantation Strategy for Facile Construction of Pt-Based Hybrid Electrocatalyst to Accelerate Oxygen Reduction Reaction, *Mater. Today Energy*, 2022, **24**, 100919, DOI: **10.1016/j.mtener.2021.100919**.

18 P. Guo, B. Liu, Y. K. Dai, X. F. Gong, Y. F. Xia, Y. L. Zhang, B. Liu, L. Zhao, X. L. Sui and Z. B. Wang, Coupling Fine Pt Nanoparticles and Co–N$_x$ Moiety as a Synergistic Bi-Active Site Catalyst for Oxygen Reduction Reaction in Acid Media, *J. Colloid Interface Sci.*, 2022, **613**, 276–284, DOI: **10.1016/j.jcis.2022.01.042**.

19 D. Shin, S. Bhandari, M. F. Tesch, S. A. Bonke, F. Jaouen, S. Chabbra, C. Pratsch, A. Schnegg and A. K. Mechler, Reduced Formation of Peroxide and Radical Species Stabilises Iron-Based Hybrid Catalysts in Polymer Electrolyte Membrane Fuel Cells, *J. Energy Chem.*, 2022, **65**, 433–438, DOI: **10.1016/j.jechem.2021.05.047**.

20 A. K. Mechler, N. R. Sahraie, V. Armel, A. Zitolo, M. T. Sougrati, J. N. Schwämmlein, D. J. Jones and F. Jaouen,

Stabilization of Iron-Based Fuel Cell Catalysts by Non-Catalytic Platinum, *J. Electrochem. Soc.*, 2018, **165**(13), F1084–F1091, DOI: **10.1149/2.0721813jes**.

21 M. Chen, C. Li, B. Zhang, Y. Zeng, S. Karakalos, S. Hwang, J. Xie and G. Wu, High-Platinum-Content Catalysts on Atomically Dispersed and Nitrogen Coordinated Single Manganese Site Carbons for Heavy-Duty Fuel Cells, *J. Electrochem. Soc.*, 2022, **169**(3), 034510, DOI: **10.1149/1945-7111/ac58c7**.

22 X. Li, Y. He, S. Cheng, B. Li, Y. Zeng, Z. Xie, Q. Meng, L. Ma, K. Kisslinger, X. Tong, S. Hwang, S. Yao, C. Li, Z. Qiao, C. Shan, Y. Zhu, J. Xie, G. Wang, G. Wu and D. Su, Atomic Structure Evolution of Pt–Co Binary Catalysts: Single Metal Sites versus Intermetallic Nanocrystals, *Adv. Mater.*, 2021, **33**(48), 1–11, DOI: **10.1002/adma.202106371**.

23 X. Ao, W. Zhang, B. Zhao, Y. Ding, G. Nam, L. Soule, A. Abdelhafiz, C. Wang and M. Liu, Atomically Dispersed Fe–N–C Decorated with Pt-Alloy Core-Shell Nanoparticles for Improved Activity and Durability towards Oxygen Reduction, *Energy Environ. Sci.*, 2020, **13**(9), 3032–3040, DOI: **10.1039/d0ee00832j**.

24 A. Serov, K. Artyushkova, N. I. Andersen, S. Stariha and P. Atanassov, Original Mechanochemical Synthesis of Non-Platinum Group Metals Oxygen Reduction Reaction Catalysts Assisted by Sacrificial Support Method, *Electrochim. Acta*, 2015, **179**, 154–160, DOI: **10.1016/j.electacta.2015.02.108**.

25 M. M. Hossen, K. Artyushkova, P. Atanassov and A. Serov, Synthesis and Characterization of High Performing Fe–N–C Catalyst for Oxygen Reduction Reaction (ORR) in Alkaline Exchange Membrane Fuel Cells, *J. Power Sources*, 2018, **375**, 214–221, DOI: **10.1016/j.jpowsour.2017.08.036**.

26 A. Serov, K. Artyushkova and P. Atanassov, Fe–N–C Oxygen Reduction Fuel Cell Catalyst Derived from Carbendazim: Synthesis, Structure, and Reactivity, *Adv. Energy Mater.*, 2014, **4**(10), 1301735, DOI: **10.1002/aenm.201301735**.

27 L. Delafontaine, E. Murphy, S. Guo, Y. Liu, T. Asset, Y. Huang, J. Chen, I. Zenyuk, X. Pan and P. Atanassov, Synergistic Electrocatalytic Syngas Production from Carbon Dioxide by Bi-Metallic Atomically Dispersed Catalysts, *ChemElectroChem*, 2022, **9**(17), e202200647, DOI: **10.1002/celc.202200647**.

28 E. Murphy, Y. Liu, I. Matanovic, S. Guo, P. Tieu, Y. Huang, A. Ly, S. Das, I. Zenyuk, X. Pan, E. Spoerke and P. Atanassov, Highly Durable and Selective Fe- and Mo-Based Atomically Dispersed Electrocatalysts for Nitrate Reduction to Ammonia via Distinct and Synergized NO$_2$ – Pathways, *ACS Catal.*, 2022, **12**(11), 6651–6662, DOI: **10.1021/acscatal.2c01367**.

29 E. Murphy, Y. Liu, I. Matanovic, Y. Huang, A. Ly, S. Guo, W. Zang, X. Yan, I. Zenyuk, E. Spoerke and P. Atanassov, Elucidating Electrochemical Nitrate and Nitrite Reduction over Atomically-Dispersed Transition Metal Sites, *Nat. Commun.*, 2023, **2**, 4–6, DOI: **10.1038/s41467-023-40174-4**.

30 T. Zhao, Y. Li, J. Liu, X. Wang, J. Zhang, C. Liu, W. Xing and J. Ge, Highly Dispersed L$_{12}$-Pt$_3$Fe Intermetallic Particles Supported on Single Atom Fe–N–C Active Sites for Enhanced Activity and Durability towards Oxygen Reduction, *Chin. Chem. Lett.*, 2022, 107824, DOI: **10.1016/j.cclet.2022.107824**.

31 X. Zhou, L. Chen, G. E. Sterbinsky, D. Mukherjee, R. R. Unocic and S. L. Tait, Pt-Ligand Single-Atom Catalysts:

Tuning Activity by Oxide Support Defect Density, *Catal. Sci. Technol.*, 2020, **10**(10), 3353–3365, DOI: **10.1039/c9cy02594d**.

32 S. Tian, B. Wang, W. Gong, Z. He, Q. Xu, W. Chen, Q. Zhang, Y. Zhu, J. Yang, Q. Fu, C. Chen, Y. Bu, L. Gu, X. Sun, H. Zhao, D. Wang and Y. Li, Dual-Atom Pt Heterogeneous Catalyst with Excellent Catalytic Performances for the Selective Hydrogenation and Epoxidation, *Nat. Commun.*, 2021, **12**(1), 1–9, DOI: **10.1038/s41467-021-23517-x**.

33 S. T. Dix, S. Lu and S. Linic, Critical Practices in Rigorously Assessing the Inherent Activity of Nanoparticle Electrocatalysts, *ACS Catal.*, 2020, **10**(18), 10735–10741, DOI: **10.1021/acscatal.0c03028**.

34 S. Rudi, C. Cui, L. Gan and P. Strasser, Comparative Study of the Electrocatalytically Active Surface Areas (ECSAs) of Pt Alloy Nanoparticles Evaluated by Hupd and CO-Stripping Voltammetry, *Electrocatalysis*, 2014, **5**(4), 408–418, DOI: **10.1007/s12678-014-0205-2**.

35 H. Yoon, H. J. Song, B. Ju, K. Jang and D. W. Kim, Gas-Phase Synthesis of PtMo Alloy Electrocatalysts with Enhanced Activity and Durability for Oxygen Reduction Reaction, *ACS Sustainable Chem. Eng.*, 2022, **10**(46), 15319–15327, DOI: **10.1021/acssuschemeng.2c05246**.

36 A. Hassan, A. Carreras, J. Trincavelli and E. A. Ticianelli, Effect of Heat Treatment on the Activity and Stability of Carbon Supported PtMo Alloy Electrocatalysts for Hydrogen Oxidation in Proton Exchange Membrane Fuel Cells, *J. Power Sources*, 2014, **247**, 712–720, DOI: **10.1016/j.jpowsour.2013.08.138**.

37 Y. Luo, B. Kirchhoff, D. Fantauzzi, L. Calvillo, L. A. Estudillo-Wong, G. Granozzi, T. Jacob and N. Alonso-Vante, Molybdenum Doping Augments Platinum–Copper Oxygen Reduction Electrocatalyst, *ChemSusChem*, 2018, **11**(1), 193–201, DOI: **10.1002/cssc.201701822**.

38 H. Luo, K. Wang, F. Lin, F. Lv, J. Zhou, W. Zhang, D. Wang, W. Zhang, Q. Zhang, L. Gu, M. Luo and S. Guo, Amorphous MoO_x with High Oxophilicity Interfaced with PtMo Alloy Nanoparticles Boosts Anti-CO Hydrogen Electrocatalysis, *Adv. Mater.*, 2023, **35**(29), 1–9, DOI: **10.1002/adma.202211854**.

39 E. Hornberger, T. Merzdorf, H. Schmies, J. Hübner, M. Klingenhof, U. Gernert, M. Kroschel, B. Anke, M. Lerch, J. Schmidt, A. Thomas, R. Chattot, I. Martens, J. Drnec, P. Strasser and E. Hornberger, Impact of Carbon N-Doping and Pyridinic-N Content on the Fuel Cell Performance and Durability of Carbon-Supported Pt Nanoparticle Catalysts, *ACS Appl. Mater. Interfaces*, 2022, **14**(16), 18420–18430, DOI: **10.1021/acsami.2c00762**.

40 U. A. Paulus, T. J. Schmidt, H. A. Gasteiger and R. J. Behm, Oxygen Reduction on a High-Surface Area Pt/Vulcan Carbon Catalyst: A Thin-Film Rotating Ring-Disk Electrode Study, *J. Electroanal. Chem.*, 2001, **495**(2), 134–145, DOI: **10.1016/S0022-0728(00)00407-1**.

41 K. M. Palanivelu, V. Prabhakaran, V. K. Ramani and K. Ramanujam, Controlling the Nitrogen Content of Metal–Nitrogen–Carbon Based Non-Precious-Metal Electrocatalysts via Selenium Addition, *J. Electrochem. Soc.*, 2015, **162**(6), F475–F482, DOI: **10.1149/2.0101506jes**.

42 Thin Film RRDE Technique for Oxygen Reduction Reaction, Probing Fuel Cell Electrocatalyst Properties with Rotating Disk and Rotating Ring-Disk Electrodes, 2008, pp. 1–5.